WELDING RESEARCH

SUPPLEMENT TO THE *WELDING JOURNAL*, AUGUST 1996
Sponsored by the American Welding Society and the Welding Research Council

A Theoretical Study on Electrical and Thermal Response in Resistance Spot Welding

The influence of contacting force on the formation of the weld nugget is investigated

BY S.-J. NA AND S.-W. PARK

ABSTRACT. The effect of contact resistance including constriction and contamination resistance has been a major hurdle for the thermoelectrical analysis of the resistance spot welding process. In this paper, a simple model was suggested and used for calculating the electrical and thermal response of the resistance spot welding process to investigate the influence of contacting forces on the formation of weld nuggets. The electrode surface of the contact interface was assumed to be axisymmetric and its microasperities to have a trapezoidal cross-section. These microasperities were considered as the one-dimensional contact resistance elements in the finite element formulation. The contamination film was assumed to be a nonconducting oxide layer, which is very brittle, so that it is broken to some number of pieces when a contacting pressure is being applied. The crushed films were assumed to be distributed at regular intervals and to conserve their size and number during the welding process. The simulation results revealed that the proposed model can be successfully used to predict the effect of the contact resistance on the electrical and thermal response of the resistance spot welding process.

S.-J. NA is a Professor and S.-W. PARK is a Senior Researcher, Dept. of Precision Engineering and Mechatronics, Korea Advanced Institute of Science and Technology, Taejon, Korea.

Introduction

Because of its light weight and ease of manufacturing, sheet metal is commonly used in industry. For effective application, rapid and low-cost joining processes are necessary for various kinds of sheet metal. From this point of view, the resistance spot welding process is a very attractive joining method (Refs. 1–5), since it is relatively simple in principle and requires minimum operator skill. Although some studies (Refs. 6–15) were carried out on the numerical analysis of the resistance welding process, to the best of the authors' knowledge, there is no paper which explicitly considers the effect of microcontacts (or contact resistance) because of its complexity and difficulty for modeling.

KEY WORDS

RSW
Temperature Distribution
Contact Resistance
Dynamic Resistance
Sheet Metal
FEM
Simulation
Thermoelectric Model
Experimental Results
Welding Cycle

This study attempts to model and analyze the resistance spot welding process of sheet metals. For this purpose, a theoretical thermoelectrical model was developed which takes into account the thermoelectric interaction at the sheet-to-sheet and electrode-to-sheet interface. A hybrid approach was suggested to explicitly include the effect of microcontacts for calculating the distribution of electrical potential and temperature in the resistance spot welding process.

The contamination film was assumed to be the insulating oxide layer, which is distributed uniformly in the contact interface. Moreover, it was assumed that the oxide contamination layer is so brittle that it is crushed to pieces as soon as the contacting pressure is applied. The broken films were then assumed to be of a certain size and were distributed in the contact interface at regular intervals. The broken film is also assumed to retain its size and number during the welding process. The microcontact in the electrode-to-workpiece and workpiece-to-workpiece interface was assumed to be a ring element with the trapezoidal cross-section. By adopting these assumptions, the constriction resistance of the single microcontact, which has insulating oxide pieces in the contact interface, can be determined by using the solution of the multiple line contact model (Ref. 16). In the hybrid approach, the mi-

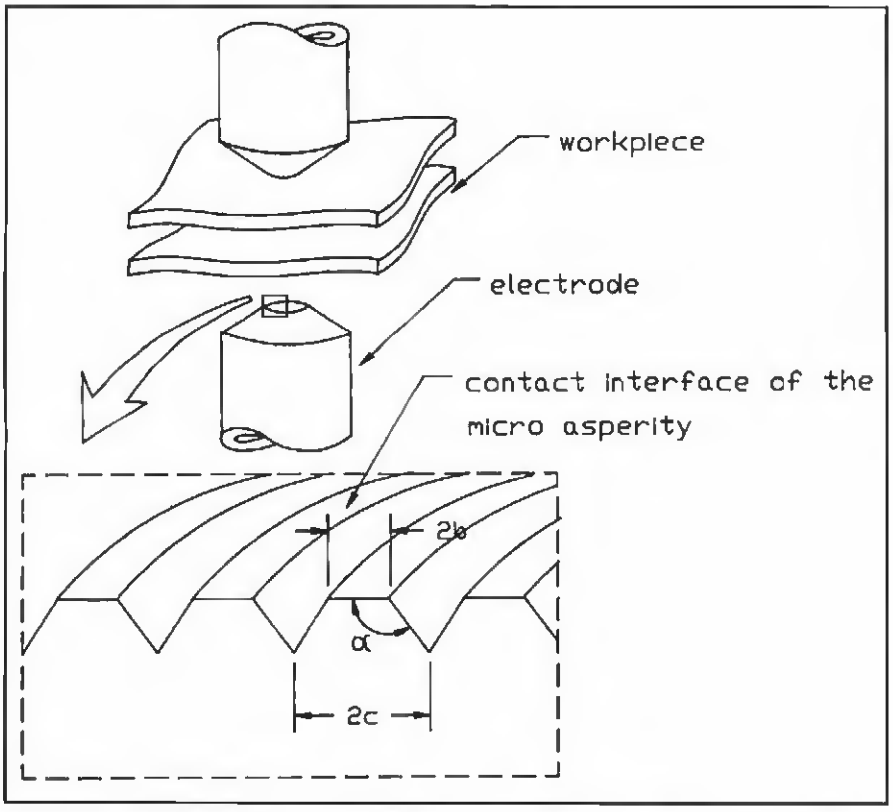

Fig. 1 — Schematic illustration of spot welding process.

crocontacts in the contact interface zone were considered as one-dimensional resistance elements related to the electrical resistance, which have no connection with the thermal behavior of the model. The conducting bodies, except the microcontact region, were meshed with axisymmetrical triangular two-dimensional elements for the finite element method. The comparison of the simulation results with the experimental ones revealed that the suggested simple model could fairly well predict the thermal response of the resistance spot welding process, although some assumptions were introduced from past experience.

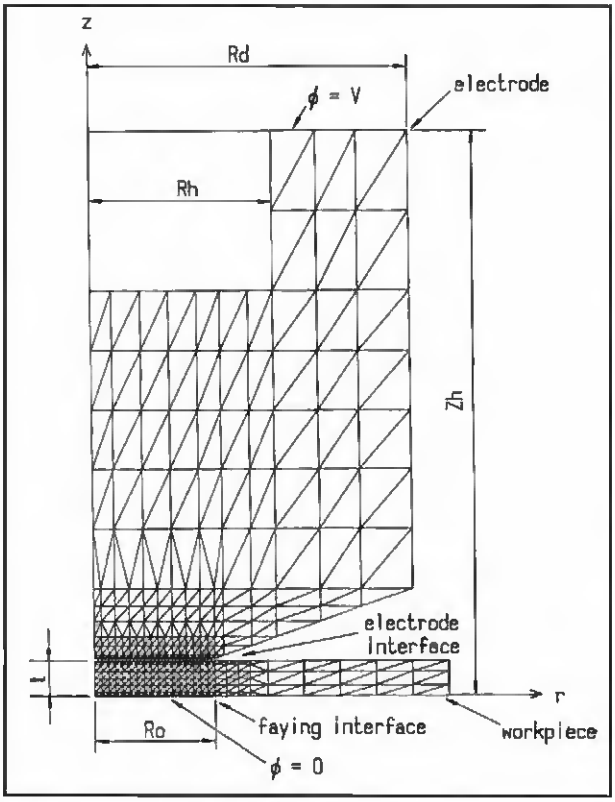

Fig. 2 — Finite element mesh generation and boundary condition in electrode and workpiece.

Modeling

The resistance spot welding process contains two copper electrodes and a pair of weldment sheets. It is schematically represented in Fig. 1. The contact surface at the sheet-to-sheet and electrode-to-sheet was assumed to be axisymmetric and its microasperities to have a trapezoidal cross-section.

Electrical Phenomena

Finite element formulation

The finite element method is a powerful tool for solving field problems. In comparison to the analytical analysis, one important merit of this method is that it can be easily applied to the model, which includes the nonuniform material properties and/or complex boundaries. In this paper, the voltage potential and temperature distribution were calculated using the finite element method.

The governing equation of the voltage potential problem for the steady-state condition, having no charge source, is well known as follows:

$$\nabla\left(\frac{1}{\rho}\nabla\Phi\right) = 0 \qquad (1)$$

where ρ is the electrical resistivity and Φ the voltage potential. This governing equation can be changed to the finite element equation using the normal finite element formulation procedure (Ref. 17). In general, this element equation can be described in the following equation:

$$[K]\{\Phi\} = \{F\} \qquad (2)$$

where [K] is called the stiffness matrix and {F} the force vector. The electrode and workpiece, except for the region of microcontacts, were meshed with the two-dimensional axisymmetrical element of the triangular cross-section, and the microcontacts were meshed with the one-dimensional element, Figs. 2 and 3. The boundary condition of the analysis domain was selected as follows:

$$\Phi = 0: 0 < r < R_o, \; z = 0 \qquad (3)$$

$$\Phi = V: R_h < r < R_d, \; z = Z_h \qquad (4)$$

$$\frac{\partial\Phi}{\partial\eta} = 0: \; \textit{other surfaces} \qquad (5)$$

where R_0 is the radius of faying interface, which was assumed to be of the size of the electrode contact surface, R_h the inner radius of electrode, R_d the outer radius of electrode, Z_h the height of the analysis domain, and n the outer normal vector to the boundary surface — Fig. 2. The total number of the element was 746, which consists of 647 two-dimensional elements and 99 one-dimensional ones. These two types of elements are ex-

plained specifically below.

One-Dimensional Element of Contact Resistance

For modeling the mechanical behavior of the contamination layer, it was assumed that the contamination film is crushed to a number of pieces which are distributed in the contact interface at regular intervals and that the size and number are unchanged during the welding process. To do this, the relationship between the asperity deformation and contact pressure must be determined in advance. It is nearly impossible, however, to consider the actual rough surface exactly in calculations because of its complexity (Ref. 18). Therefore, the surface of the contact interface was assumed to be axisymmetric and the microasperities to have a trapezoidal cross-section. These microasperities (or microcontacts) act as one-dimensional resistance elements in the finite element formulation. The width of the microasperity 2c and space angle α would be determined by choosing the roughness data — Fig. 1. For calculations, 0.1 mm and 135 deg were chosen as the value of 2c and α, respectively. The width of the microcontact interface zone 2b and the asperity height h have the same geometrical relationship as in the authors' previous paper (Ref. 19), if it is assumed that α is kept to be constant during the deformation. In this paper, the assumptions and results of the reference (Ref. 20) were used for determining the relationship between the microasperity deformation and contact pressure. By adopting these assumptions, the real contact size in the microasperity 2b and nominal contact pressure P_n have the following relationship:

$$b = \frac{P_n}{H + P_n} \cdot c \tag{6}$$

where H is the hardness of the contacting body (Ref. 21), which is a function of temperature. Hence, the distribution of the degree of contact n = b/c along the r-direction would have a very close relation to the contact pressure distribution.

By using the assumption that the initially broken contamination film retains its size and number during welding, the size of the micrometal bridge e can be determined as follows — Fig. 4:

$$e = \frac{b - \Sigma f_o}{n_f} = \frac{b - f_o \cdot n_f}{n_f} \tag{7}$$

where f_0 is the size of the individual broken film and n_f the number of metal bridges or broken film — Fig. 4. In this study, 4.75 x 10^{-4} mm and 20 were adopted for f_0 and n_f, respectively, which resulted in the maximum e value of 2.025 x 10^{-3} mm for the case of b = c (n = 1). Substituting equation 6 for Equation 7,

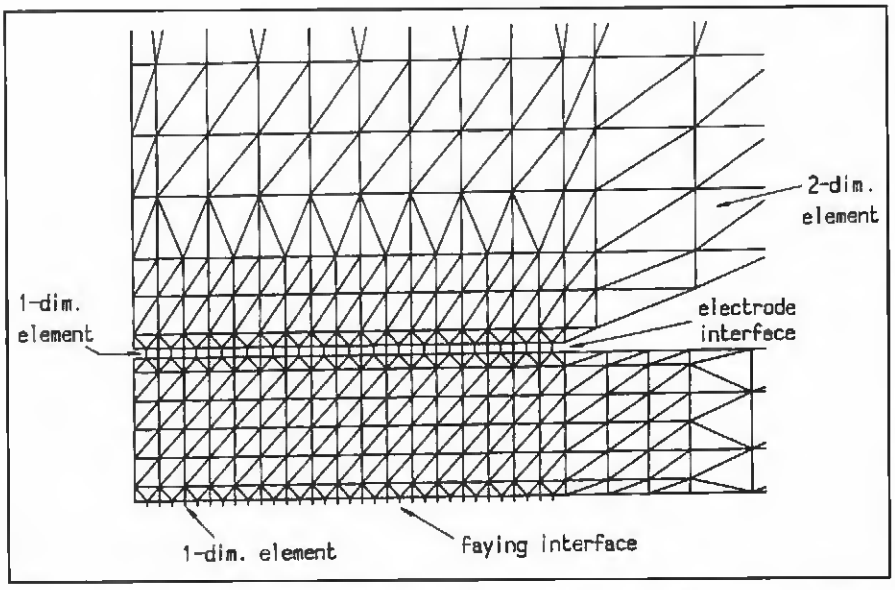

Fig. 3 — Detailed view of mesh generation around contact interface zone.

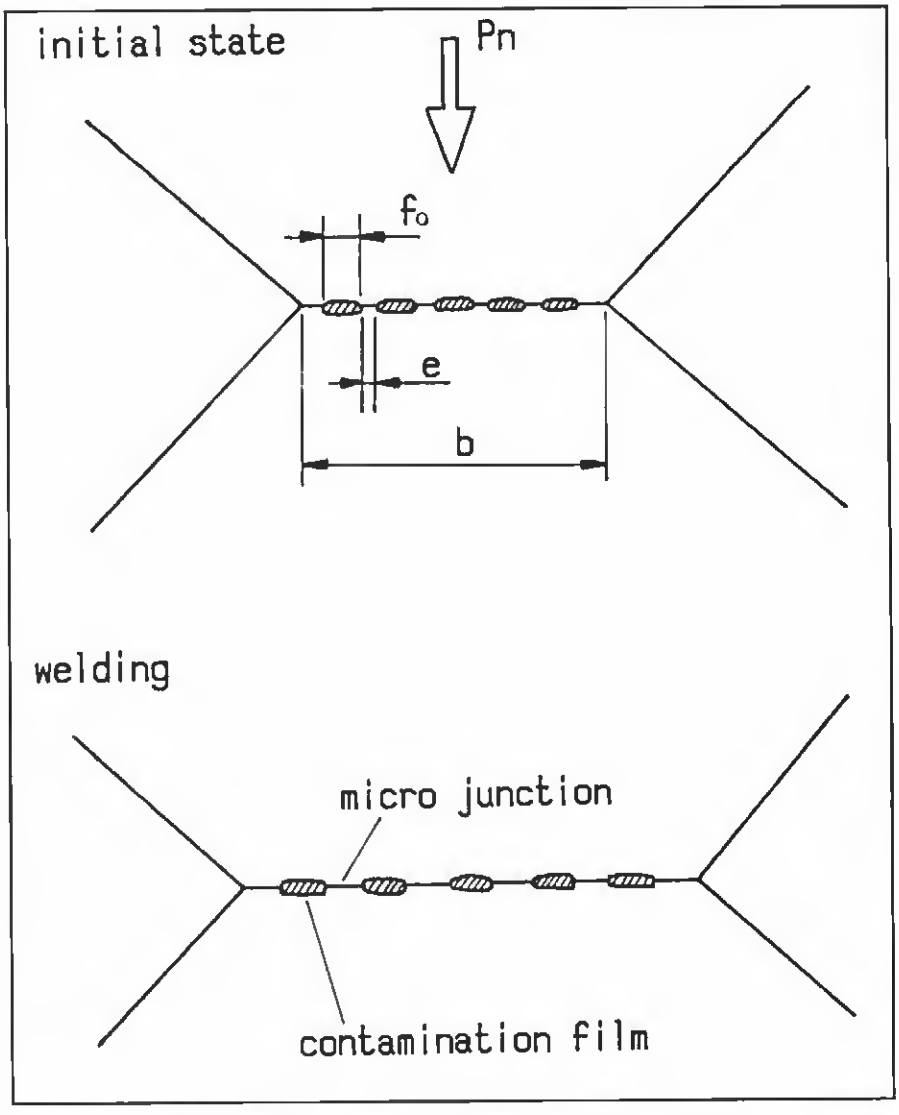

Fig. 4 — Conceptual illustration of contamination film model.

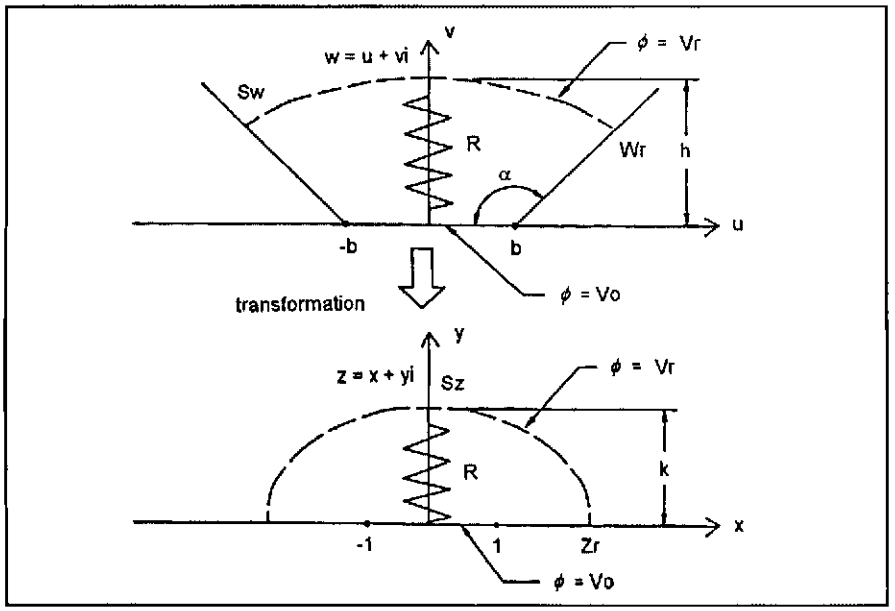

Fig. 5 — Schematic illustration of mapping method for modeling contact resistance.

the size of the micrometal bridge e can be then calculated from the data of contact pressure by using the following formula:

$$e = \frac{P_a}{(H+P_a)} \cdot \frac{c}{n_f} - f_o \tag{8}$$

The contact resistance of any microasperity R was determined for unit thickness by adopting the analytical solution of the multiple-line contact with the given space angle. In this study, the contact resistance between the contact interface and any voltage reference point was analytically calculated by using the conformal mapping method as mentioned in Ref. 16. Using the Schwarz-Christoffel transformation (Ref. 22), any position of the angled surface in the w-plane can be transformed into a position of the flat surface in the z-plane — Fig. 5. The mapping function adopted in this study is expressed as follows:

$$\frac{dw}{dz} = \frac{2b \cdot \Gamma\left(\frac{1}{2}+\frac{\alpha}{180}\right)}{\Gamma\left(\frac{1}{2}\right)\cdot\Gamma\left(\frac{\alpha}{180}\right)} \cdot \left(1-z^2\right)^{\left(\frac{\alpha}{180}\right)-1} \tag{9}$$

where Γ is the gamma function. By using this mapping function, the width of any microcontact e in the physical plane (transformed plane) is converted into g in the computational plane (transformed plane). In the same manner, the distance between two microcontacts in the physical plane q_{ij} is changed into d_{ij}, and the voltage reference point W_r into Z_r. The relationship between the physical and computational coordinate can be obtained by integrating Equation 9, *i.e.*,

$$w = \frac{2b \cdot \Gamma\left(\frac{1}{2}+\frac{\alpha}{180}\right)}{\Gamma\left(\frac{1}{2}\right)\cdot\Gamma\left(\frac{\alpha}{180}\right)} \int_0^z \left(1-\xi^2\right)^{\left(\frac{\alpha}{180}\right)-1} d\xi \tag{10}$$

In the simulation, the point in the computational plane (z-plane) corresponding to a selected point in the physical plane (w-plane) can be calculated by applying a method of trial and error to the numerical complex integration. In this study, the trial value is z, and w is a known value; if the trial value z satisfies equation 10, the selected z value is considered as the mapping point at the computational plane corresponding to the point w.

In the computational plane, the value obtained by summing up the potential drops generated by the separate currents is the same as the potential drop between any microcontact and the voltage reference surface S_z like the electrostatic charge distribution problem, *i.e.*,

$$\sum_{j=1}^{n_i} r_{ij} I_j = \Delta V_i \tag{11}$$

where r_{ij} ($i \neq j$) is the so-called mutual resistance, r_{ii} the self-resistance, I_j the current flowing through the j-th microcontact, and ΔV_i the potential drop between the i-th microcontact and the voltage reference surface S_z. The mutual resistance can be obtained by considering the microcontact as the area-less line charge, and the self-resistance by using the analytical results of the single contact (Refs. 23–25), *i.e.*,

$$r_{ii} = \frac{\rho}{\pi} \cdot ln \left[2\left|Z_r\right|/g + \sqrt{\left(2\left|Z_r\right|/g\right)^2 - 1} \right] \tag{12}$$

$$r_{ij} = \frac{\rho}{\pi} \cdot ln\left[\left|Z_r\right|/d_{ij}\right] \quad (i \neq j) \tag{13}$$

Here $|Z_r|$ is the average distance between the microcontact and voltage reference point Z_r and ρ is the electrical resistivity. In this study, it was assumed that the potentials at all microcontacts in the interface region are uniform, *i.e.*, $\Delta V_i = \Delta V$ = constant. These assumptions are sufficiently grounded, because the size of any microcontact is, in general, very small compared to the size of the conducting body and the voltage reference point can be selected so as to be much larger than the width of the interface region. Hence, the current flow through any microcontact I_j, according to any given value of ΔV can be obtained by solving the simultaneous equations of Equation 11. The contact resistance R (that is, the electrical resistance between the interface region and voltage reference surface per unit length) of the multiple line contact can be then defined as follows:

$$R = \frac{\Delta V}{\sum_{i=1}^{n_i} I_i} \tag{14}$$

Because the potential at the voltage reference point in the physical plane and the total current $\sum_{i=1}^{n_i} I_i$ are not changed by the geometrical transformation, the constriction resistance of the multiple line contact having any space angle can be calculated by using this conformal mapping method.

The joule heat generation rate at the microasperity q_M can be easily determined by using the contact resistance R, which is determined from Equation 14, and the voltage drop across the asperity ΔV as follows:

$$q_M = \frac{\left|V_r - V_o\right|^2}{R} = \frac{\Delta V^2}{R} \tag{15}$$

where ΔV can be determined from the voltage potential distribution calculated by the finite element method. Finally, the contact resistance R can be applied to determining the element stiffness matrix in the finite element formulation of the governing equation of the voltage potential problem:

$$[K] = \frac{r_i + r_j}{2} \cdot \frac{1}{R}\begin{bmatrix} 1 & -1 \\ -1 & 1 \end{bmatrix} \tag{16}$$

where r_i and r_j are the radial positions of

the i-th and j-th nodes in the one-dimensional elements.

Two-Dimensional Element

The conducting bodies, except the region of microcontacts (or microasperities), were meshed with the two-dimensional axisymmetric elements with the triangular cross-section. In this element, the element stiffness matrix of the voltage potential problem can be described as follows (Ref. 26):

$$[K] = \frac{(r_i + r_j + r_k)}{12\Delta} \cdot \rho \begin{bmatrix} b_i b_i + c_i c_i & b_i b_j + c_i c_j & b_i b_k + c_i c_k \\ & b_j b_j + c_j c_j & b_j b_k + c_j c_k \\ \text{symmetric} & & b_k b_k + c_k c_k \end{bmatrix}$$

$$\text{where } b_i = z_j - z_k,\ b_j = z_k - z_i,\ b_k = z_i - z_j$$
$$c_i = r_k - r_j,\ c_j = r_i - r_k,\ c_k = r_j - r_i$$
$$\Delta = \frac{\begin{vmatrix} 1 & r_i & z_i \\ 1 & r_j & z_j \\ 1 & r_k & z_k \end{vmatrix}}{2} \qquad (17)$$

and i, j, k represent the node points in any element.

Temperature Distribution

In the following section, the formulation procedure of the finite element for temperature distributions was summarized from Ref. 26 to provide a better understanding of the study. The governing equation is called the energy balance equation and is described as follows:

$$\rho_t c_t \frac{\partial T}{\partial t} = \nabla(k_t \nabla T) + \dot{Q}_t \qquad (18)$$

where ρ_t is the density, c_t the specific heat, k_t the thermal conductivity, T the temperature and $\dot{Q}_t$ the heat generation rate per volume. By using the finite element formulation, the above governing equation can be expressed as follows:

$$\left[\bar{K}\right]\{T\}_{n+1} = \left\{\bar{f}\right\}_{n+1} \qquad (19)$$

$$\text{where } \left\{\bar{f}\right\}_{n+1} = \left[(1-\theta)\left([K_c] + [K_v]\right) + \frac{1}{\Delta t}[C] \right] \{T\}_n + (1-\theta)\left(\{F_g\} + \{F_v\}\right)_n + \theta\left(\{F_g\} + \{F_v\}\right)_{n+1}$$
$$\text{and } \left[\bar{K}\right] = \theta\left([K_c] + [K_v]\right) + \frac{1}{\Delta t}[C]$$

In this relationship $[K_c]$ is the stiffness matrix of the conduction term, $[K_v]$ that of the convection term, [C] the specific coefficient matrix and $\{F_v\}$ the force vector of the convection term. The parameter θ may be chosen to give the different algorithm. In this study, θ = 1/2 was simply chosen for calculations. The joule heat generation value obtained by using the voltage potential distribution data was considered as $\{F_g\}$ vector in the above finite element equation.

The boundary conditions were determined as follows — Fig. 2:

$$\frac{\partial T}{\partial r} = 0 \qquad r = 0$$
$$\frac{\partial T}{\partial z} = 0 \qquad 0 < r < R_0,\ z = 0$$
$$-k_t \frac{\partial T}{\partial z} = h_w(T - T_w) \text{ : contact surface of cooling water}$$
$$-k_t \frac{\partial T}{\partial n} = h_\infty(T - T_\infty) \text{ : free surface} \qquad (20)$$

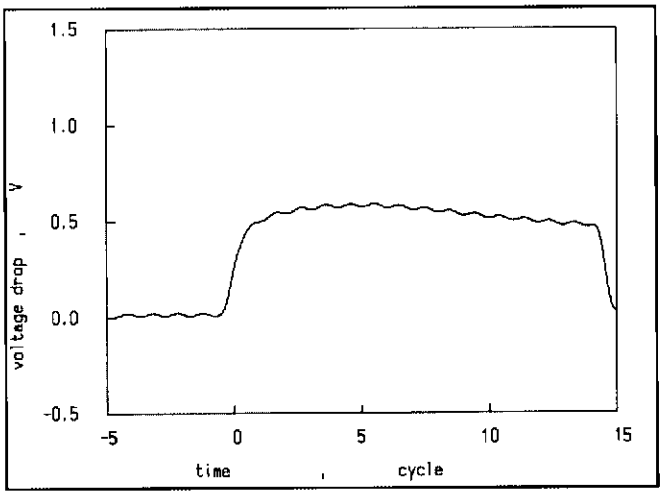

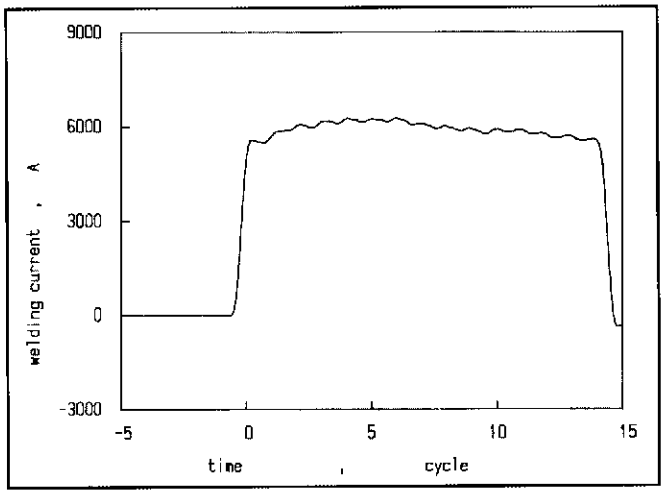

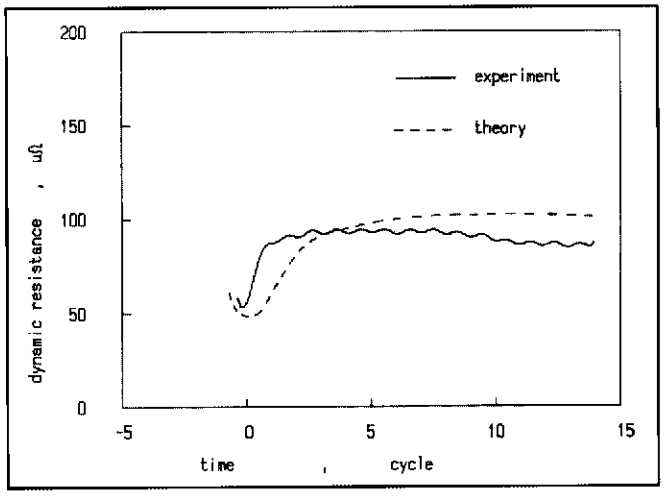

Fig. 6 — Traces of voltage drop and current between two electrodes and dynamic resistance for welding time of 15 cycles (300 kg$_f$ electrode force, 40% current setting). A — voltage drop; B — current; C — dynamic resistance.

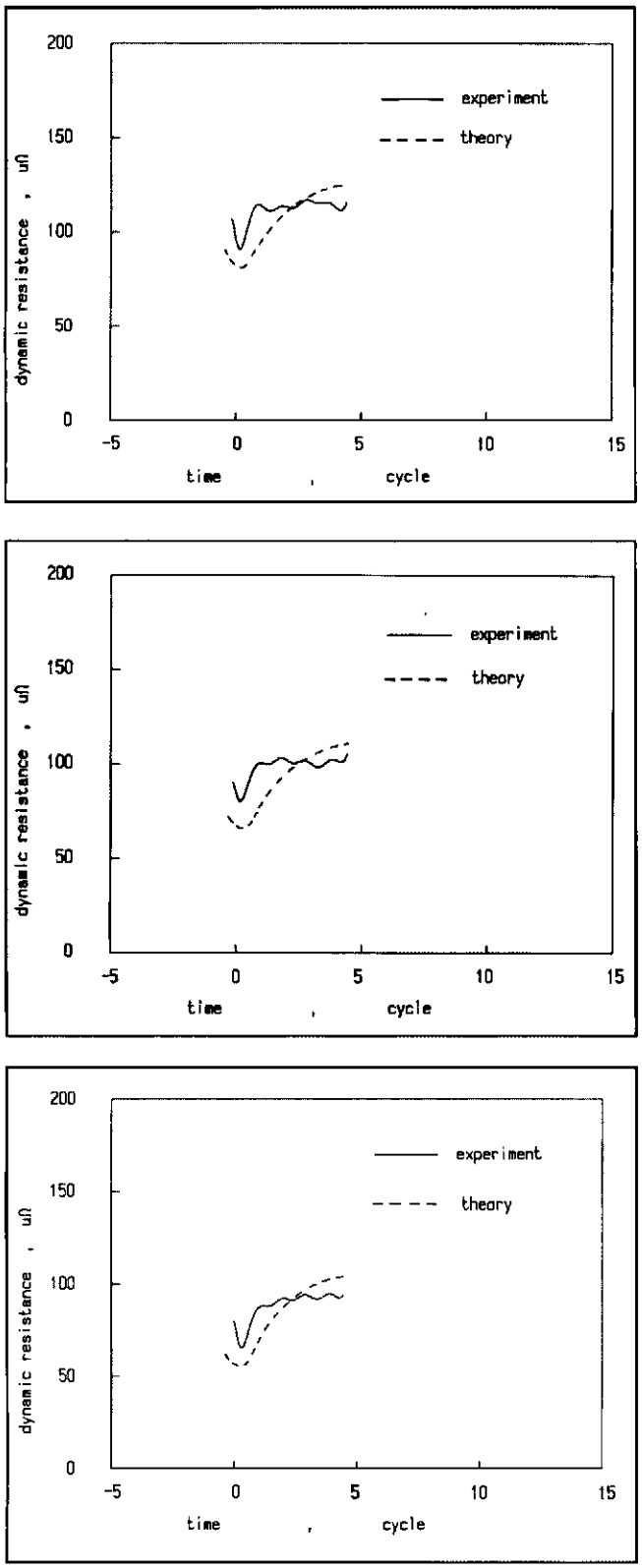

Fig. 7 — Dynamic resistance profiles for various electrode forces (5 cycles welding time, 30% current setting). A — 100 kg$_f$, B — 200 kg$_f$, C — 300 kg$_f$.

where h_w is the convective heat transfer coefficient of the cooling water, h_∞ that of the surrounding air, T_w the temperature of the cooling water and T_∞ the temperature of the surrounding air. For simulations, a RWMA Class II electrode with a tapered-flat shape and 7.0-mm-diameter contact surface was considered, and consequently, 9, 5, 3.5, 23.5 and 1.5 mm were chosen as R_d R_h R_o Z_h and t, respectively. For calculating the temperature distribution, it is required that the matrix [C] of the one-dimensional element should be determined. In this study, the volume of the one-dimensional element v, which was used for calculating the specific coefficient matrix [C], was approximated by considering the trapezoidal shape of the microasperity and Equation 6 as follows:

$$v = 2\pi r\left[1-\left(\frac{P_n}{H+P_n}\right)^{\gamma}\right]\cdot\frac{c^2}{\tan(\alpha-\pi/2)} \quad (21)$$

Experiments

A three-phase direct current spot welding machine was used for experiments. A toroidal coil, data acquisition circuit and personal computer were used for measuring the current profile. The voltage drop across two electrodes was also measured to provide the input data of the computer simulation by using the contact probes, data acquisition circuit and personal computer. Before beginning the welding process, the preset electrode force was confirmed by using the hydraulic force measuring unit.

For verifying and analyzing the theoretical model of the hybrid finite element method, which considered the contamination film effect, a number of experiments were performed. At first, the dynamic resistance of the welding process was measured and compared with the simulation results. Three levels of the contacting force and three types of the welding time were considered for welding conditions. The experimental results of the temperature distributions were also compared with the simulation ones for various contacting forces and welding times. For determining the isothermal lines of the fusion and heat-affected zones, the weldments were cross-sectioned, polished and macroetched.

Results and Discussion

Dynamic Resistance

With the proposed hybrid approach, the variation of dynamic resistance which has been frequently referred to as a good process variable for monitoring the resistance spot weld quality could be predicted. The dynamic resistance was defined as the value of the voltage drop between two electrodes divided by the overall current flowing through the workpiece.

Figure 6A and B show the traces of the voltage drop across two electrodes and welding current measured during the welding time of 15 cycles under the condition of 300-kg_f contacting force and 40% current setting. The dynamic resistance was simulated and measured for the same condition and the results were compared in Fig. 6C. In the first one to two cycles, the dynamic resistance decreased very steeply and reached its minimum value. This phenomenon is probably due to the effect of the contamination films and fresh asperities existing in the workpiece-to-workpiece interface and/or workpiece-to-electrode interfaces. The fact that the dynamic resistance then increased gradually along the welding time is probably due to the electrical resistivity of the workpiece, which increased with the increasing temperature. To the contrary, the hardness of the material made the contact resistance decrease as the temperature increased, because the hardness value of the material decreased, and consequently the asperities in the contact surfaces were easily deformed with the increasing temperature. From these results, it could be concluded that in simulations the effect of electrical resistivity to increase the contact resistance is more dominant than the effect of material hardness to decrease the contact resistance. The dynamic resistance measured, however, decreased gradually along with the welding time, which resulted in an increasing discrepancy between the simulated and measured values. Most of the errors seen both in the dynamic resistance and temperature distribution (discussed later) are probably due to the errors in estimating the contact resistance, such as the line element approach and axisymmetrical microasperity.

Figure 7A–C shows the variation of dynamic resistance profiles for contacting forces of 100 kg_f, 200 kg_f and 300 kg_f with the condition of the five cycles welding time and 30% current setting. A notable fact in the experimental results was that in the case of low electrode force, there was a relatively large deviation in the dynamic resistance. When the electrode force was not high enough to sufficiently break down the surface waviness, the inconsistent fit-up of the electrode-to-workpiece and workpiece-to-workpiece at each weld could cause a considerable variation in the dynamic resistance profiles. In this study, the effect of the surface waviness which would result in the inconsistent fit-up was not considered in the contact resistance model. When the weld was made at 300 kg_f, which is close to the contacting force value recommended by RWMA, the measured dynamic resistance profile could be predicted fairly well by the pro-

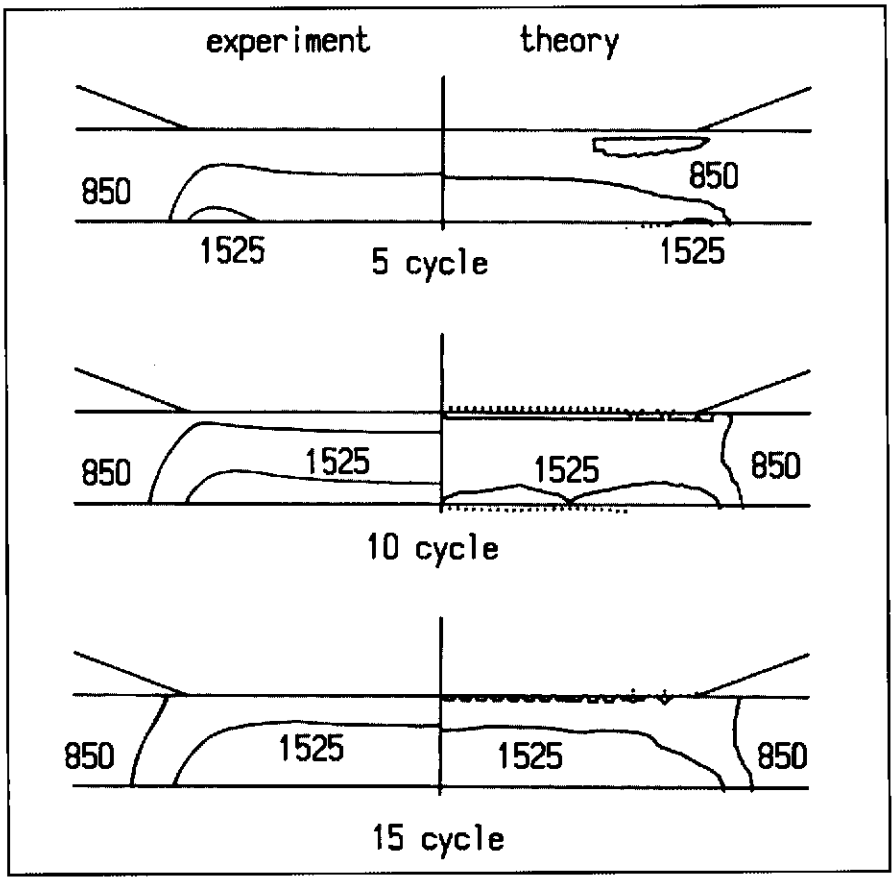

Fig. 8 — Isothermal lines of melted and heat-affected zone boundary for various welding times (300 kg_f electrode force, 40% current setting).

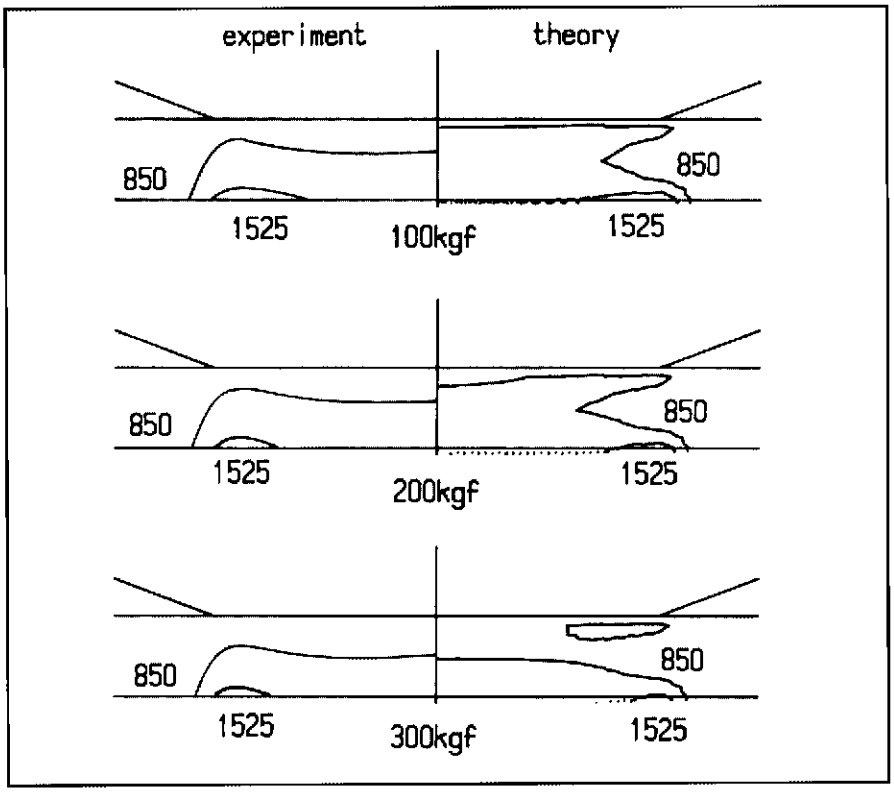

Fig. 9 — Isothermal lines of melted and heat-affected zone boundary at welding time of five cycles for various electrode forces (40% current setting).

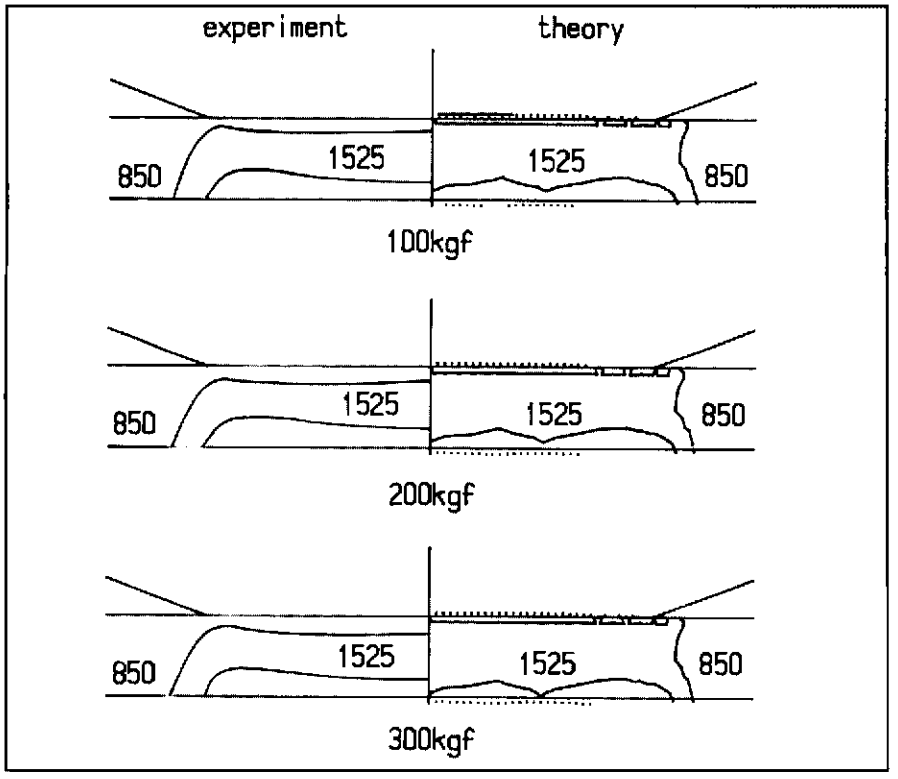

Fig. 10 — Isothermal lines of melted and heat-affected zone boundary at welding time of 10 cycles for various electrode forces (40% current setting).

posed model. These results revealed that in the low force range it is not sufficient to consider only the contamination film, because of the surface inconsistence (waviness, etc.) which prevents the full contact. In the relatively high contacting force range, however, considerably satisfying results could be obtained by using the proposed hybrid approach, which considered the contamination film effect.

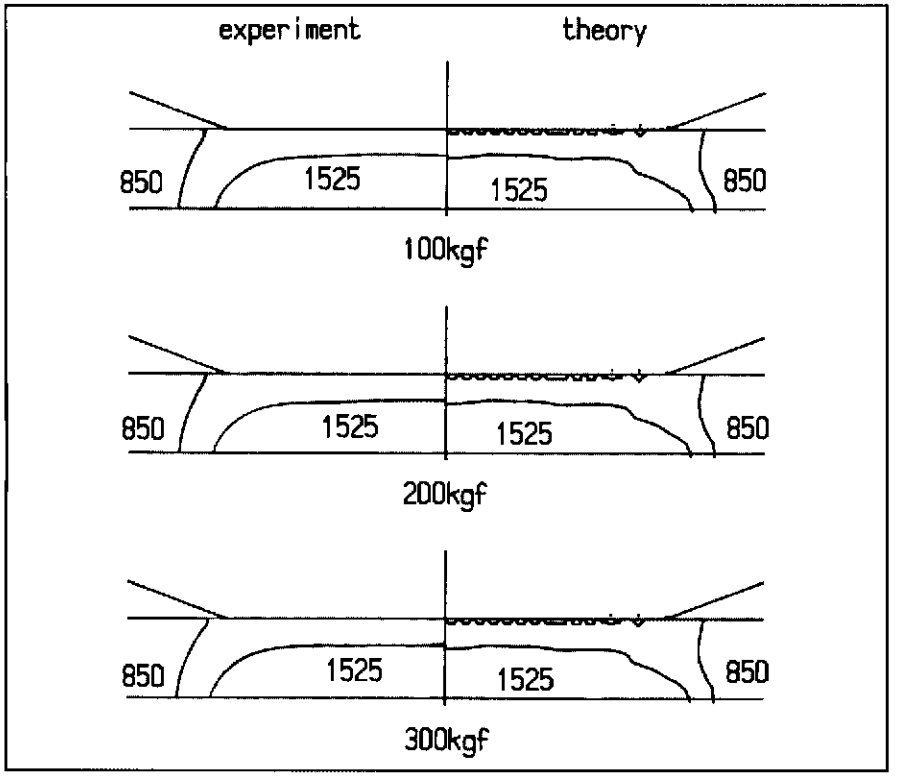

Fig. 11 — Isothermal lines of melted and heat-affected zone boundary at welding time of 15 cycles for various electrode forces (40% current setting).

Temperature Distribution

For verifying the proposed hybrid finite element model of the spot welding process, the experimental results of the temperature distribution were compared with the simulation ones. The temperature of the melting zone boundary was assumed to be 1525°C for the 0.08% carbon steel used, which had a thickness of 1.5 mm. In resistance spot welding, the austenitic transformation temperature will be elevated because of its relatively high heating rate. Therefore, the temperature of the heat-affected zone (HAZ) boundary was assumed to be 850°C instead of 723°C (Ref. 27).

The electrical resistivity, thermal conductivity, specific heat and hardness of mild steel and copper are known to vary with the temperature. In order to incorporate these variations into the simulation, those parameters were cited from data in the *Metals Handbook* (Ref. 28). For the phase change problem, the method proposed by Landau and Lifshitz (Ref. 29) was employed. That is, during fusion, the specific heat was assumed to be the value of the latent heat divided by the temperature range between the liquidus and solidus temperature.

Figure 8 represents the isothermal lines of the melting and HAZ boundary for various welding times of 5, 10 and 15 cycles under the condition of 300 kg_f contacting force and 40% current setting. In the case of five cycles, there was only a small torus-shaped melted region at the workpiece-to-workpiece interface. When the welding cycle increased, the melted region became larger and consequently had the nugget shape. Although two results seemed to agree well in the case of 10 and 15 cycles, the difference between the experimental and simulation results were not small for the short welding time of five cycles. This is probably due to the initial inconsistency in the model of the contact phenomena. When the electrode force was not high enough to break down the surface waviness sufficiently, the fit-up of the electrode-to-workpiece and workpiece-to-workpiece becomes inconsistent at each weld. In this study, however, the effect of the surface waviness, which caused the inconsistent fit-up, was not considered in the contact resistance model and consequently in the hybrid finite element approach. The thickness and width of the melted region were slightly bigger in ex-

perimental results than in simulated ones, though the region of the 850°C isothermal line was smaller in the experiment for the case of 10 and 15 cycles condition. This phenomenon is probably related to the fact that the experimental values of the dynamic resistance were generally greater than the simulation values. That is, in simulations, less joule heat was considered at the interface region. Therefore, most of these errors are also due to the assumptions adopted in the contact resistance model such as the line element approach and axisymmetrical microasperity.

Figures 9–11 represent the temperature distribution for various contacting forces (100 kg_f, 200 kg_f, 300 kg_f) and 40% current setting with the welding time of 5, 10 and 15 cycles. In three cases, the increase in contacting force decreased the size of the melted region. However, this phenomenon became weaker when the welding cycle was longer. If the welding time was longer than 10 cycles, the size of the melted region seemed to be almost the same in the three contacting forces mentioned. This result revealed that the effect of the contact pressure is meaningful only when the microasperities exist, because it is each asperity that is deformed by the contact pressure and introduces the contact resistance in the proposed model. As the welding cycle increased, however, the number of the fully deformed asperities (in the real situation, these were perhaps already melted) increased, that is, the number of the pressure sensitive asperities (*i.e.*, the contact resistance elements) decreased. This is considered to be the reason why the effect of the contact pressure and contact resistance was sensitive to the temperature distribution when the welding cycle was short. On the whole, the result of experiments revealed that the size of the melted region decreases when the contacting force increases in the low force level condition, and that the temperature response of the spot welding process can be successfully predicted by using the proposed hybrid finite element approach, which considers the contamination film effect.

Conclusion

The effect of the contacting force, microasperity and contamination film on the electrical and temperature response in resistance spot welding was analyzed and discussed by using a hybrid finite element model. In this model, the analytical solution of the constriction resistance for multiple line contacts and the approximation of the asperity deformation were adopted to consider the effect of microcontacts in calculating the potential and temperature distribution by using the finite element method. For verifying the proposed model, a number of experiments were performed for various welding conditions. The results of the simulation and experiment revealed that the effect of the electrode force on the temperature distribution in resistance spot welding is considerable when many deformable asperities exist in the contact surface; therefore, they cannot be ignored. Moreover, this hybrid finite element approach can be applied to many other allied processes such as electrical contact devices and thermal contact problems.

References

1. Johnson, I. W. 1960. Spot welding of carbon steel. *Welding Journal* 39(3): 89-s to 96-s.

2. Lovell, D. T., and Anderson, C. N. 1964. Process and design criteria for resistance welding Rene 41. *Welding Journal* 43(7): 307-s to 319-s.

3. Kelly, J., and Knowlson, P. M. 1967. The BWRA quality monitor and spot-welding galvanized steel — an evaluation. *Welding Journal* 46(3):114-s to 120-s.

4. Patange, S. R., Anjaneyulu, I., and Reddy, G. P. 1985. Microprocessor-based resistance welding monitor. *Welding Journal* 64(12): 33–38.

5. Rokhlim, S. I., and Adler, L. 1985. Ultrasonic evaluation of spot weld quality. *Welding Journal* 64(7): 191-s to 200-s.

6. Kouwenhoven, W. B., and Sackett, W. T., Jr. 1950. The spreading resistance of contacts. *Welding Journal* 29(10): 512-s to 520-s.

7. Kouwenhoven, W. B., and Little, C. W. 1952. Contact resistance. *Welding Journal* 31(10): 457-s to 465-s.

8. Wu, K. D. 1975. Resistance spot welding of high contact — resistance surface for weld bonding. *Welding Journal* 54(10): 436-s to 443-s.

9. Ryazantsev, V. I. 1981. The true area of mechanical contact in the spot welding of aluminum alloys. *Avt. Svarka*, No. 12, pp. 43–47.

10. Tslasf, A. L. 1982. A thermophysical criterion for the weldability of electric contact material in a steady state regime. *IEEE Trans. Components, Hybrids, Manuf. Technol.*, Vol. CHMT-5, pp.147–152.

11. Eggert, G. M., and Dawson, P. R. 1986. Assessment of a thermoviscoplastic model of upset welding by comparison to experiment. *Int. J. Mech. Sci.*, Vol. 28, pp. 563–589.

12. Nied, H. A. 1984. The finite element modeling of the resistance spot welding process. *Welding Journal* 63(4): 123-s to 132-s.

13. Houchens, A. F., and Page, R. E. 1977. Numerical modeling of resistance spot welding. *ASME W.A.M., Numerical Modeling of Manufacturing Process*, pp. 117–129.

14. Satoh, T., Katayama, J., and Ahe, H. 1969.Temperature distribution and breakdown of oxide layer during resistance spot welding using two-dimensional model. Document No. III 371-69, Annual Assembly of IIW., Kyoto, Japan.

15. Tsai, C. L., Jammal, O. A., Papritan, J. C., and Dickinson, D. W. 1992. Modeling of resistance spot weld nugget growth. *Welding Journal* 71(2): 47-s to 54-s.

16. Park, S.-W., and Na, S.-J. 1988. Determination of current density distribution and constriction resistance in the multiple line contact with various space angles by using conformal mapping. *IEEE Trans. Components Hybrids and Manuf Technol.*, Vol. CHMT-11, pp.314–317.

17. Huebner, K. H., and Thorton, E. A. 1982. *The Finite Element Method for Engineers*, 2nd ed., John Wiley & Sons, Inc. 18. Bay, N., and Wanheim, T. 1976. Real area of contact between a rough tool and a smooth workpiece at high normal pressures. *Wear*, Vol. 38, pp. 225–234.

19. Park, S.-W., and Na, S.-J. 1990. A study on hybrid modeling of electrical phenomena in contacts. *IEEE Trans. Components Hybrids and Manuf Technol.*, Vol. CHMT-13, pp. 326–330.

20. Pullen, J., and Williamson, J. B. P. 1972. On the plastic contact of rough surfaces. *Proc. R. Soc.* (A), Vol. 295, pp. 300–319.

21. Tabor, D. 1951. *The Hardness of Metals*, Oxford Univ. Press.

22. Carrier, G. F., Krook, M., and Pearson, C. E. 1966. *Function of a Complex Variable*, McGraw-Hill, N. Y.

23. Molnar, I., and Lelovics, G. 1980. The behavior of line contacts upon the effect of fault currents. *IEEE Trans. Components Hybrids and Manuf Technol.* Vol. CHMT-3, pp.191–195.

24. Baycura, O. M. 1969. Contact resistance determination by a point-slope method. *IEEE Trans. Ind. Gen. Appl.*, Vol. IGA-5, pp. 208–211.

25. Sano, Y. 1985. Effect of space angle on constriction resistance and contact resistance for the case of line contact. *IEEE Trans. Components Hybrids and Manuf Technol*, Vol. CHMT-8, pp. 228–234.

26. Nied, H. A., and Schlansker, C. A. 1984. The thermo structural analysis of electric contacts using a finite element model. *IEEE Trans. Components Hybrids and Manuf. Technol.*, Vol. 7, pp. 112–124.

27. Feuerstein,W. J., and Smith, W. K. 1954. Elevation of critical temperature in steel by high heating rates. Trans. ASM, Vol. 46, pp.1270–1281.

28. *Metals Handbook*, 9th ed., Vol. 1, ASM International, Materials Park, Ohio.

29. Landau, L. D., and Lifshitz, E. M. 1960. *Electrodynamic of Continuous Media*, Pergamon Press.